Materials Research Express

PAPER • **OPEN ACCESS**

Growth of nonpolar a-plane AlGaN epilayer on Al-composition graded-AlGaN buffer layer and characterization of its surface morphology and crystalline quality

To cite this article: Abbas Nasir *et al* 2022 *Mater. Res. Express* **9** 105004

Materials Research Express

OPEN ACCESS

RECEIVED
28 July 2022

REVISED
21 September 2022

ACCEPTED FOR PUBLICATION
13 October 2022

PUBLISHED
31 October 2022

PAPER

Growth of nonpolar a-plane AlGaN epilayer on Al-composition graded-AlGaN buffer layer and characterization of its surface morphology and crystalline quality

Abbas Nasir[1,*], **Bin Xu**[1], **Irshad Ali**[2] and **Jehan akbar**[3,*]

[1] School of Electronic and Optical Engineering, Nanjing University of Science and Technology, 200 Xiaolingwei, Nanjing, 210094, People's Republic of China
[2] PhD Scholar at the School of Biological Sciences and Medical Engineering, Southeast University Nanjing, People's Republic of China
[3] Glasgow College, University of Electronic Science and Technology of China, Chengdu China, Department of Physics, Hazara University Mansehra, KPK, Pakistan
[*] Authors to whom any correspondence should be addressed.

E-mail: abbasnasir02@gmail.com and Jehan.akbar@glasgow.ac.uk

Keywords: atomic force microscopy, MOCVD, polarization indirect microscopic imaging, Al composition graded AlGaN buffer layer

Abstract

Metal-organic chemical vapor deposition was successfully used to grow un-doped nonpolar *a*-plane AlGaN on an *r*-plane sapphire substrate. High-resolution x-ray (HR-XRD), atomic force microscopy, Polarization Indirect Microscopic Imaging, and Hall effect measurement were used to investigate the effect of the nonpolar *a*-plane AlGaN layer on the graded AlGaN buffer layer. The results reveal that inserting the AlGaN-graded layer improves the crystalline quality and morphology of the surface. The root means the square value was less than 1.47 nm, while the background electron concentration was -3.9×10^{17} cm^{-3}. In addition, the HR-XRD full width at half maximum indicates improved crystalline quality.

1. Introduction

In the last decade, AlGaN-based semiconductors have attracted considerable attention. High-power transistors, laser diodes, and light-emitting diodes (LEDs) in the visible or ultraviolet range are some applications for which it is commonly utilized [1, 2]. Because of the stable physical and chemical characteristics, AlGaN-based materials have a wide application prospect. Significant progress has been achieved in enhancing the working efficiency of AlGaN-based LEDs by optimizing the crystalline quality, doping efficiency, and device design [3]. AlGaN was also often utilized as a light source in the deep ultraviolet spectrum in applications, including medical tools disinfection [3], purification of water [4], medical diagnostics, and photo-therapy [5]. Nonpolar *a*-plane AlGaN LEDs, however, have various challenges with their performance, including low crystalline quality, technical issues, and threading dislocation densities [6]. Due to the hetero-epitaxial growth of the nonpolar AlGaN-based LEDs on a substrate of sapphire or SiC, threading dislocations (TDs) and stacking defects [7, 8] are often generated. Commercial LEDs are prohibitively costly because of the exorbitant cost of the AlGaN prototypes developed on MOCVD at high temperatures. On the other way, reactive magnetron sputtering shows attractive low-cost LEDs for fabricating large-scale AlGaN LEDs. Few groups tried to grow a high-temperature AlN template with high output light and external quantum efficiency, but the biggest issue for an AlGaN LED is threading dislocation, external quantum efficiency (EQE), internal quantum efficiency (IQE), etc [9].

It has been found that many methods can change threading dislocation density and enhance crystalline quality. The Al composition change leads to the bandgap, spontaneous width, piezoelectric polarization, and lattice constant of the alloy. These properties [10] can be controlled through alloy composition [11, 12], which is vastly used to fabricate active and functional layers of electronic nitride devices. Furthermore, Inserting AlGaN graded layer improves the crystal quality and morphology of the surface [12, 13].

The importance of the graded AlGaN buffer layer on the un-doped nonpolar a-plane AlGaN layer with increasing nonpolar a-plane AlGaN layer growth time has been investigated in this study. The structural and morphological characteristics of the un-doped nonpolar a-plane AlGaN epilayers were studied using high-resolution x-ray diffraction (HR-XRD), atomic force microscopy (AFM), and Polarization Indirect Microscopic Imaging. According to the results, introducing the Al composition graded AlGaN buffer layer enhances the crystalline quality and surface morphology of the un-doped nonpolar *a*-plane AlGaN epilayers.

2. Experimental work

Nonpolar *a*-plane AlGaN samples A_1, A_2, A_3, and A_4, were grown on a 2-inch *r*-plane sapphire substrate at a low pressure of 40 T using metalorganic chemical vapor deposition (MOCVD) technique on a graded AlGaN buffer layer. The graded buffer layer and high-temperature HT-AlN nucleation layer, on the other hand, were produced. The sources of Ga, Al, and N were trimethyl-gallium (TMGa), trimethyl-aluminum (TMAl), and ammonia (NH3). The carrier gas was hydrogen (H_2) [14, 15]. Before the growth, to reduce surface impurities, the *r*-plane is heated to 1080 °C for 5 min. Then it was heated for two minutes at a temperature of 1080 °C in NH_3 and H_2 ambiance for nitration treatment. Then the 100 nm HT-AlN nucleation layer was deposited on the sapphire substrate at 1130 °C after the nucleation layer; the graded AlGaN layer was deposited with different Al compositions and the same temperature as a buffer layer. Finally, the graded buffer layer deposited the nonpolar *a*-plane AlGaN with the same composition and different growth times. Specifically, all four samples from A_1 to A_4 were grown with the same graded layer of the un-doped AlGaN buffer layer.

On the other hand, the Polarization Indirect Microscopic Imaging system is developed by modifying a traditional optical far-field microscope. Imaging was then obtained by analyzing the dependency of the optical intensity transmitted through or reflected from the sample under test so that the variation of the polarisation status of incident light could be precisely controlled, because of the intensity variations caused by the polarizer's rotation.

The following equation can be used to describe the intensity of the CCD:

$$I = \frac{I_0}{2}[1 + \sin 2(\alpha - \phi)\sin\delta] \tag{1}$$

Where α is the incident angle, I_0 is the unpolarized intensity, and ϕ is the polarization angle, usually known as the angle along the sluggish vibration axis, and δ is the optical retardation.

If we trigonometrically extend equation (1), we obtained,

$$I = \frac{1}{2}1_0 + \frac{1}{2}I_0 \sin\delta \cos 2\phi \sin 2\alpha + \frac{1}{2}I_0 \sin\delta \sin 2\phi \cos 2\alpha \tag{2}$$

Following the matching by the defined parameters, we may be using the equation:

$$I_i = a_0 + a_1 \sin\alpha + a_2 \cos\alpha \tag{3}$$

A comparison of equations (2) and (3) gives us:

$$a_0 = \frac{1}{2}I_0, \quad a_1 = \frac{1}{2}I_0 \sin\delta \cos 2\phi, \quad a_2 = -\frac{1}{2}I_0 \sin\delta \sin 2\phi \tag{4}$$

A total of 360° of polarization can be achieved by rotating it. and then the angles N = 360° a_0, a_1, and a_2 are calculated:

$$a_0 = \sum_{i=1}^{N}\frac{1}{N}I_i, \; a_1 = \sum_{i=1}^{N}\frac{2}{N}I_i \sin a_i, \; a_2 = \sum_{i=1}^{N}\frac{2}{N}I_i \sin a_i \tag{5}$$

Using these parameters, we can find our desired quantities as:

$$I_{dp} = a_0, \; \sin\delta = \frac{a_1^2 + a_2^2}{a_0}, \; \phi = \frac{1}{2}\arccos\left(\frac{(a_1^2 + a_2^2)^{\frac{1}{2}}}{a_0}\right) \tag{6}$$

The Stokes parameters were determined by applying equation (6) to the Jones and Muller model, which is given by equation (7).

$$S_0 = I_{dp}\,(1 + \sin\delta) = E_{0x}^2 + E_{0y}^2$$

$$S_1 = I_{dp}(1 + \sin\delta)\cos 2\phi = E_{0x}^2 - E_{0y}^2$$

$$S_2 = 2\sqrt{I_{dp}}\,(1 + \sin\delta)\cos 2\phi = 2E_{0x}E_{0y}\sin\delta$$

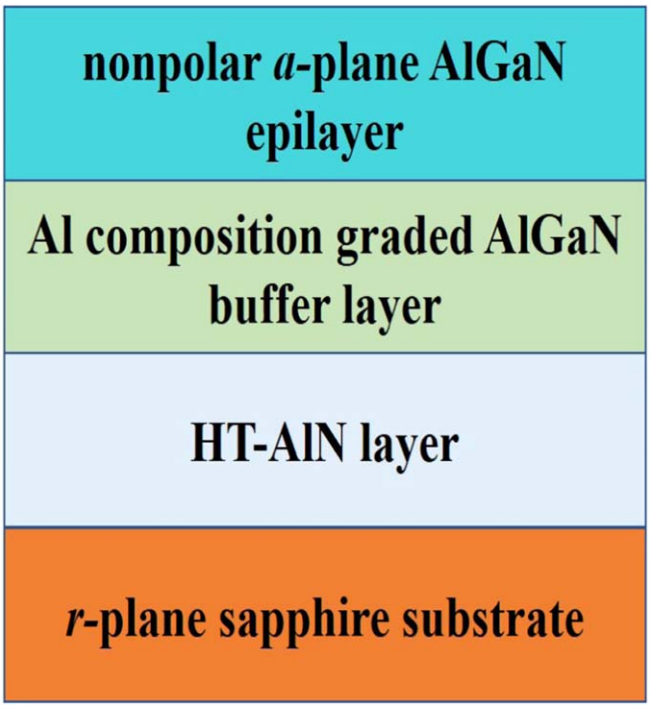

Figure 1. The schematic diagram of a-plane AlGaN with graded-AlGaN layer.

$$S_3 = 2\sqrt{I_{dp}}(1 + \sin\delta)\sin 2\phi = 2E_{0x}E_{0y}\cos\delta \tag{7}$$

Field intensities were acquired at each CCD pixel after the linear polarization field was impinged from 0 to 2 and fitted at each pixel using equation (3). I_{dp}, sin δ, and Ø have been calculated from the fitting curve by using equations (4)–(6) after the curve has been fitted. We estimated the Stokes parameters using these derived numbers as stated by equation (7). The electric field components' amplitudes in the x and y directions are denoted by the letters E_{0x} and E_{0y}. Optical retardation, also ∅ known as the phase shift between these orthogonal electric field components, occurs. According to equation (6), I_{dp} is the average of all polarisation intensities.

Due to the polarization modulation in PIMI, the intensity variation at each spatial point that the PSF encompasses can be expressed sinusoidally. Additionally, we can verify whether the spatial point of the experimental data adheres to the coupling principle as stated in equation (3). According to applicable criteria such as adjusted root square, the data points that follow the near-to-far field coupling principle fit well with equation (3), and those that do not are filtered out as noise. As a result, the optical diffraction limit is broken, and the PSF's breadth is reduced.

The sample was cut into quadrates with a diameter of 1×1 cm^2 following the growth. HR-XRD was utilized to determine the crystallinity and Al composition, while AFM and PIMI were employed to examine the surface roughness and thickness of the material. Then a 180 s-long annealing process was conducted at 300 °C in the air to obtain Ohmic contact. The Hall effect measurement in this study was performed using an Ecopia system with a magnetic field of 0.35 T to characterize the electrical properties of the nonpolar *a*-plane AlGaN epilayers at room temperature using the van der Pauw method. Figure 1 shows the schematic layer diagram with increasing nonpolar *a*-plane AlGaN growth time from 6 to 24 min in the different experiments.

3. Results and discussion

A nonpolar *a*-plane AlGaN layer was grown for 24 min to study how a graded layer affects the surface and crystalline quality of the sample. All subsequent samples were grown under the same circumstances with an increasing time of 6 min for each sample. HR-XRD, AFM, and PIMI characterization techniques were employed to check the crystalline quality and surface morphology.

Figure 2 describes the HR-XRD 2θ–ω curve of sample A_1. This curve shows two peaks with different peak values, $2\theta = 57.64$ degrees and $2\theta = 59.28$ degrees, confirming the oriented nonpolar *a*-plane AlGaN layer and nonpolar *a*-plane AlN layers [16–18]. As a result, the HR-XRD curve representing sample A_1 looks very much like the curve representing sample A_1–A_4, which is excluded from the figure where the composition of Al is 0.27 for all samples. Furthermore, the full width at half maximum (FWHM) XRC curves for samples A_1–A_4 of

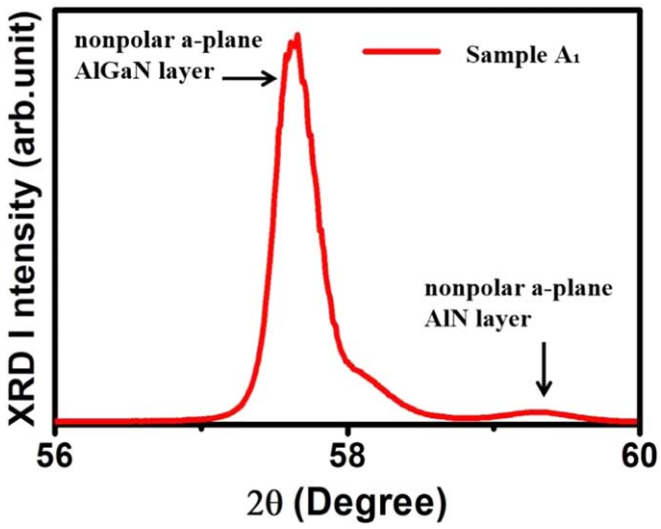

Figure 2. The HR-XRD 2θ–ω scanning curve of the A_1 a-plane AlGaN sample.

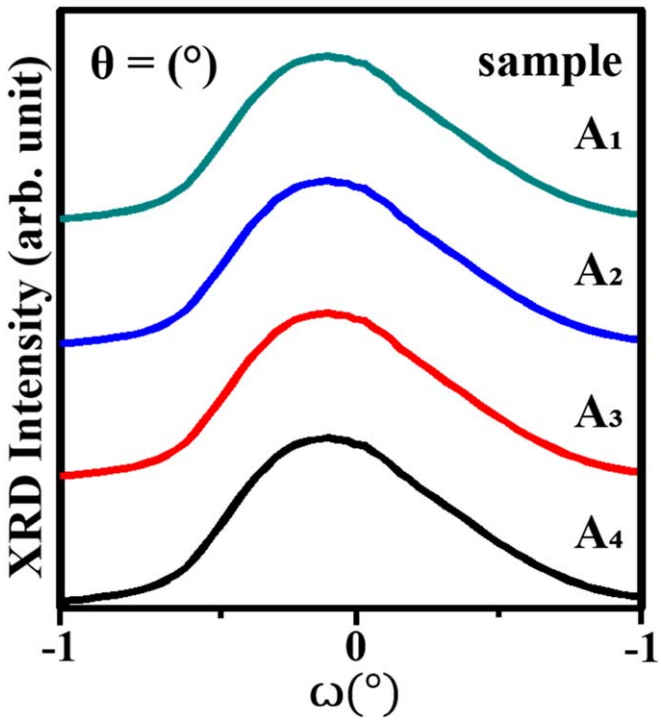

Figure 3. The XRC curves for all the samples A_1–A_4 of nonpolar a-plane AlGaN, along the [0001] axis.

nonpolar *a*-plane AlGaN epilayer are shown in figure 3, measured and summarized in table 1. It can be seen that the values of A_2, A_3, and A_4 are smaller than the value of A_1, indicating that the nonpolar *a*-plane AlGaN growth time has a significant effect on the graded AlGaN buffer layer. The phenomenon may be explained by increasing the growth time of the nonpolar *a*-plane AlGaN epilayer on the graded AlGaN buffer layer, which influences the climb or slide of the residual strain dislocation and simplifies defect contact and extinction, as a result of the crystalline quality has improved [19–21]. As shown in figure 3, the FWHM value gradually decreased from 1101 arcsec to 677 arcsec as the growth time of the nonpolar a-plane AlGaN layer increased. Therefore, the thickness of this layer also increased from 240 nm for sample A_1 to 470 nm for sample A_2. However, the FWHM value of XRC increased again to 964 arcsec for sample A_3 when the layer thickness further increased to 545 nm and 595 nm for sample A_4 when the growth time increased to 24 min. This result demonstrates that the Al-composition-graded AlGaN intermediate layer inserted between the HT-AlN buffer layer and nonpolar *a*-plane AlGaN

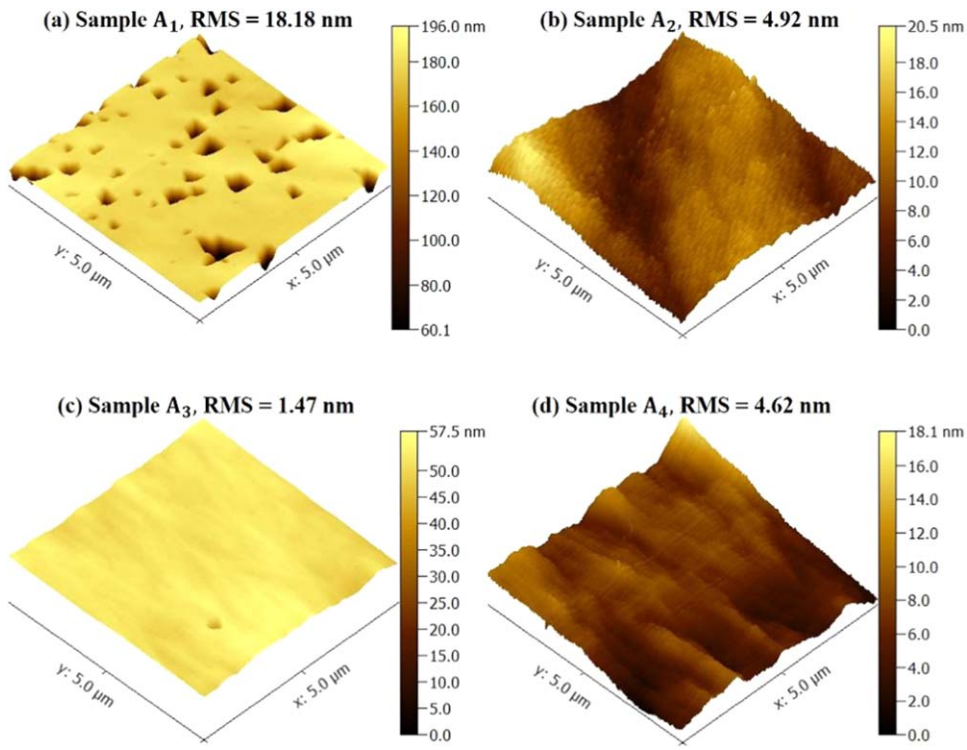

Figure 4. AFM images of four nonpolar a-plane AlGaN epilayer samples A_1–A_4 show an area of $5 \times 5\ \mu m^2$.

Table1. XRC FWHM results for all samples A_1–A_4 beside [0001] at $\varphi = 0°$ and $[1\bar{1}00]$ at $\varphi = 90°$, RMS results.

Sample	A_1	A_2	A_3	A_4
The thickness of the nonpolar AlGaN layer (nm)	240	470	545	595
FWHM (arc sec) (°)	1101	677	964	820
RMS Value (nm)	18.8	4.92	1.47	4.62

epitaxial film directly links to the dislocations density as a result of the variation in the inserted intermediate layer thickness. However, the defect density and lattice distortion may increase when the nonpolar *a*-plane AlGaN layer development time on the graded AlGaN buffer layer increases. The reduction in anisotropic strain suffered in the nonpolar *a*-plane AlGaN epilayer as a result of the enhancement in the migration capacity of the Al ad-atoms induced by the optimization of the interruption time was attributed to the remarkable improvement in crystalline quality and the significant reduction in anisotropy. Meanwhile, as the nonpolar *a*-plane AlGaN layer's growth time increases, the AlGaN epilayer's thickness can also increase, perhaps contributing to crystalline quality degradation. As shown in table 1, the FWHM is increased with the AlGaN layer's growth time.

On the other hand, AFM was used to characterize and investigate all sample's morphological properties. Figure 4 shows the larger-scale surface morphology change of the sample surface in the first sample. Table 1 shows that the surface morphology is likewise highly rough. However, as the AlGaN layer growth period rose from 6 to 12 min, the surface morphology of the second sample decreased from 18.8 nm to 4.92 nm. Furthermore, as the growth time was increased with the exact composition of Al and structure, the RMS value dropped to 1.47 nm inside a surface area of $5 \times 5\ \mu m^2$ [22]. Sample A_1 has the smoothest surface of all the samples, as evidenced in three-dimensional atomic force microscopy photos in figure 3. The decrease of residual strain in nonpolar AlGaN epilayers is often associated with improvements in surface morphology [23]. The RMS value increases again as the growth time is increased from 18 to 24 min. However, when compared to samples A2 and A3, the surface roughness of sample A4 increase again, which may be explained in principle by an increase in the thickness of the nonpolar a-plane AlGaN epitaxial layer leading to the transformation of its growth model into a 3-dimension [24]. Table 1 shows sample A_3 AFM results are the best compared to the other samples. This demonstrates that increasing the AlGaN layer's growth time significantly impacts the graded layer.

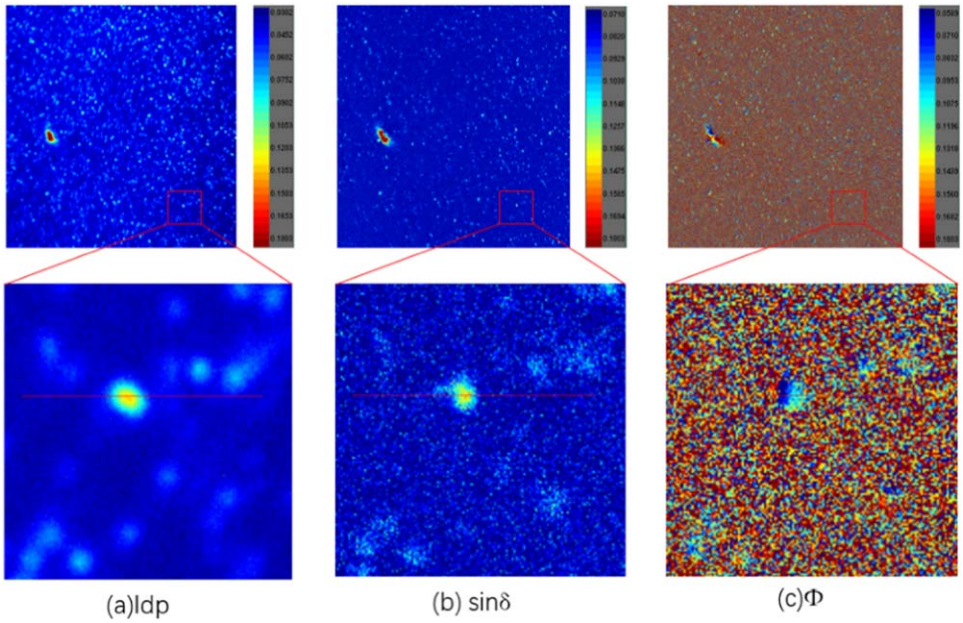

Figure 5. Defects images from (a) conventional microscope, (b) PIMI sinδ, and (c) PIMI ϕ.

PIMI (Polarization Indirect Microscopic Imaging) method is utilized in this experiment to evaluate the anisotropic characterization of defects. PIMI technology was applied to a nonpolar *a*-plane AlGaN epilayer to check the defects in the surface. This method uses a rotating polarizer to excite scattering light from 0° to 180° at a step of 18°. After being reflected from the sample surface, the reflected light will pass a quarter-wave plate orienting to 90° and a linear analyzer to 45° relative to the polarizer, respectively. Ten images are collected by a highly sensitive CCD (PiA2400-17gm, Basler) with 5 million pixels, which could achieve the pixel resolution of 34.5 nm under the 100× objective. In recently published articles [24–28], the PIMI method showed a high sensitivity for nanostructures like nanoparticles and GaN nanorods.

The sample under PIMI is shown in figure 5. Here I_{00} represents the average intensity under all polarization states, which indicates the results under a conventional microscope. Sinδ is the sine of the phase difference between two orthogonal polarization components of the scattered light, and ϕ is the polarization ellipse orientation angle of the beam reflected from the sample. The light intensity curve at the red line is shown below. A distinct area has been intercepted for further analysis in figure 6.

We can see that the FWHM for sinδ is smaller than FWHM for a conventional microscope, which is 21 pixels (724.5 nm) and 25 pixels (862.5 nm), respectively. Therefore, the image resolution is enhanced by the sinδ parameter in the PIMI method.

According to the curves for Idp and sinδ, we can quickly locate the defect with relatively low background noise. As a parameter for detecting the fast axis for the birefringence effect, the curve of ϕ is very coarse when no birefringence effect occurs on the sample surface with no defect, and the background values are completely controlled by noise when calculating the phi angle. However, a strong local birefringence effect occurs at two sides and generates a significant signal due to defect stress. The improved signal-noise ratio raised a smooth curve for ϕ at the corresponding position for defects in Idp and sinδ. In addition, the defect is in the shape of a pyramid, which means the stress directions on both sides of the defect are opposite in the X-Y plane. Different directions of the fast birefringence axis will be produced on two sides of the defect. The PIMI system well detects these sub-wavelength structural characteristics of this defect. It can be seen in figure 5(c) that the defect is divided into two parts, which realizes the resolution capability that a traditional microscope can hardly achieve.

The background electron concentration of the nonpolar *a*-plane AlGaN layer decreases to -3.9×10^{17} cm^{-3} as the growth periods of the nonpolar *a*-plane AlGaN layer increase. In contrast, the native background electron concentration drops from -10^{18} to -3.9×10^{17} cm^{-3}. It is commonly assumed that the inadvertently high background electron concentration was obtained due to oxygen impurities acting as donors to the GaN epilayers. On the other hand, the first principle predicts that when $x > 0.3$, oxygen will undergo a DX transition in $Al_xGa_{1-x}N$, serving as a big acceptor [25]. Consequently, the high background electron concentration is not attributable to contaminants in the oxygen. A reduction in background electron concentration might cause a reduction in VN density. The decrease in native electron concentration was also linked to VN, the primary carrier in GaN epilayers [26].

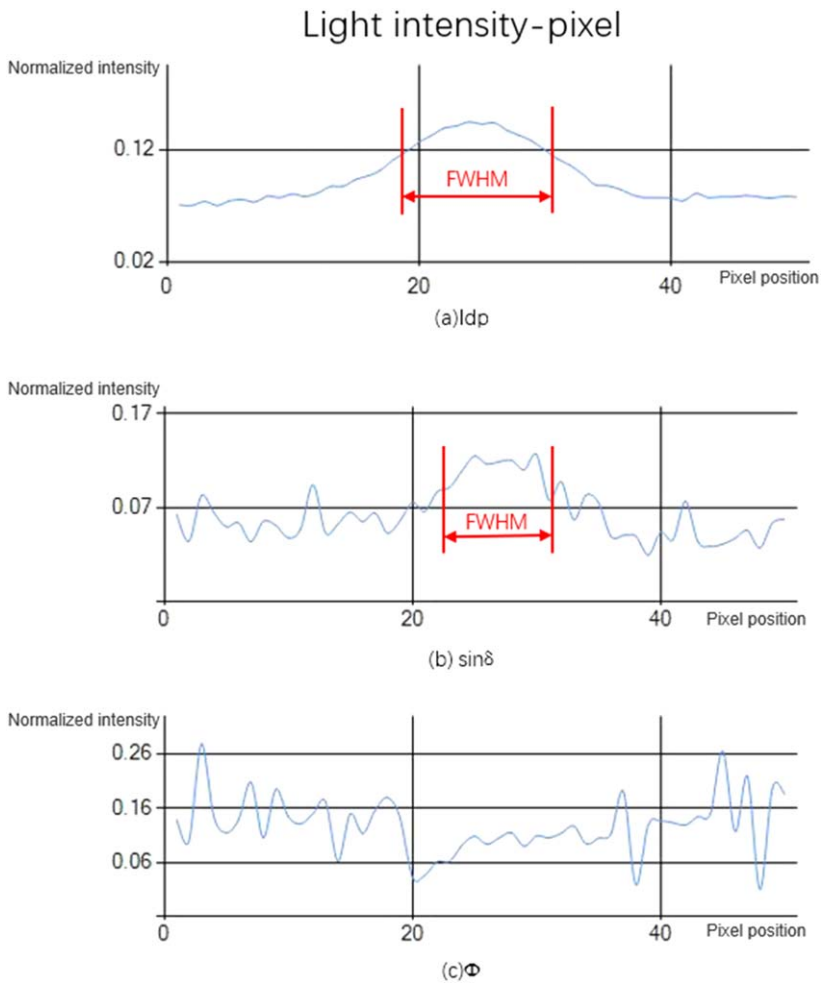

Figure 6. Characteristic curves for defects from (a) conventional microscope, (b) PIMI sinδ, and (c) PIMI ϕ.

4. Conclusion

In This study, we used a nonpolar *a*-plane AlGaN epilayer with increasing growth time, greatly affecting the surface morphology and crystalline quality. The impact of the insertion of the Al-composition-graded AlGaN intermediate layer on the crystalline quality and surface morphology of the nonpolar *a*-plane AlGaN epilayers was thoroughly investigated. As a result, an RMS value as small as 1.47 nm was obtained for the nonpolar *a*-plane AlGaN epilayer due to the reduced defect density and size of the pyramidal defects. We were able to detect the defects at a high resolution using the PIMI technology. The local birefringence effect in detects has also been detected in PIMI ϕ images. However, background electron concentrations as low as -3.9×10^{17} cm^{-3} were achieved. These results show that increasing the growth time of nonpolar *a*-plane AlGaN epilayers over a graded nonpolar a-plane AlGaN buffer layer can dramatically minimize defects and misfit dislocations.

Acknowledgments

This work was supported by the National Major Scientific Instruments and Equipment Development Project (No. 61827814), Beijing Natural Science Foundation (No. Z190018), the National Natural Science Foundation of China (No. 62105155), the Ministry of Education collaborative project (B17023).

Data availability statement

All data that support the findings of this study are included within the article (and any supplementary files).

ORCID iDs

Abbas Nasir https://orcid.org/0000-0003-2979-8848

References

[1] Cho C-Y *et al* 2012 Enhanced emission efficiency of GaN-based flip-chip light-emitting diodes by surface plasmons in silver disks *Appl. Phys. Express* **5** 122103
[2] Shur M S and Gaska R 2009 Deep-ultraviolet light-emitting diodes *IEEE Trans. Electron Devices* **57** 12–25
[3] Würtele M *et al* 2011 Application of GaN-based ultraviolet-C light emitting diodes–UV LEDs–for water disinfection *Water Res.* **45** 1481–9
[4] Chen R Z, Craik S A and Bolton J R 2009 Comparison of the action spectra and relative DNA absorbance spectra of microorganisms: information important for the determination of germicidal fluence (UV dose) in ultraviolet disinfection of water *Water Res.* **43** 5087–96
[5] Meduri N B *et al* 2007 Phototherapy in the management of atopic dermatitis: a systematic review *Photodermatology, Photoimmunology & Photomedicine* **23** 106–12
[6] Huang H-M, Wu Y-C and Lu T-C 2011 Exciton localization behaviors of basal stacking faults in a-plane AlGaN alloys *J. Electrochem. Soc.* **158** H491–5
[7] Nasir A *et al* 2019 Effects of indium surfactant and MgN intermediate layers on surface morphology and crystalline quality of nonpolar a-plane AlGaN epi-layers *Optik - International Journal for Light and Electron Optics* **192** 162978
[8] Yang Y *et al* 2021 Defect effect on the performance of nonpolar GaN-based ultraviolet photodetectors *Appl. Phys. Lett.* **118** 053501
[9] Ni R *et al* 2019 AlGaN-based ultraviolet light-emitting diode on high-temperature annealed sputtered AlN template *J. Alloys Compd.* **794** 8–12
[10] Mayboroda I *et al* 2017 Growth of AlGaN under the conditions of significant gallium evaporation: phase separation and enhanced lateral growth *J. Appl. Phys.* **122** 105305
[11] Quay R 2008 *Gallium Nitride Electronics* Vol. 96 (Springer Science & Business Media)
[12] Wang W *et al* 2018 High-performance nonpolar a-plane GaN-based metal–semiconductor–metal UV photo-detectors fabricated on $LaAlO_3$ substrates *J. Mater. Chem. C* **6** 3417–26
[13] Seredin P *et al* 2022 S2-semipolar GaN grown by HVPE on a non-polar m-plane sapphire: Features of growth and structural, morphological, and optical properties *Opt. Mater.* **129** 112507
[14] Fan A *et al* 2019 Enhanced hole concentration and improved surface morphology for nonpolar a-plane p-type AlGaN/GaN superlattices grown with indium-surfactant *Superlattices Microstruct.* **130** 396–400
[15] Wu Z *et al* 2019 Enhanced structural and electrical properties of nonpolar a-plane p-type AlGaN/GaN superlattices *Superlattices Microstruct.* **125** 310–4
[16] Yang H *et al* 2016 γ-Aminobutyric acid ameliorates fluoride-induced hypothyroidism in male Kunming mice *Life Sci.* **146** 1–7
[17] Dai Q *et al* 2017 Effects of Mg-doping on characteristics of semi-polar (112¯2) plane p-AlGaN films *Mater. Lett.* **209** 472–5
[18] Laskar M R *et al* 2011 Distorted wurtzite unit cells: determination of lattice parameters of nonpolar a-plane AlGaN and estimation of solid phase Al content *J. Appl. Phys.* **109** 013107
[19] Yu H B *et al* 2019 Advantages of AIGaN-based deep-ultraviolet light-emitting diodes with an Al-composition graded quantum barrier *Opt. Express* **27** A1544–53
[20] Laskar M R *et al* 2011 High-resolution x-ray diffraction investigations of the microstructure of MOVPE grown a-plane AlGaN epilayers *J. Cryst. Growth* **315** 208–10
[21] Hiroki M and Kumakura K 2019 Ohmic contact to AlN: Si using graded AlGaN contact layer *Appl. Phys. Lett.* **115** 4
[22] Zhao J *et al* 2016 Defects reduction in a-plane AlGaN epi-layers grown on r-plane sapphire substrates by metal-organic chemical vapor deposition *Appl. Phys. Express* **10** 011002
[23] Tao P *et al* 2016 Crack-free Al0. 5Ga0. 5N epilayer grown on SiC substrate by in situ SiNx interlayer *Mater. Sci. Semicond. Process.* **41** 291–6
[24] Tang K *et al* 2016 The roles of buffer layer thickness on the properties of the ZnO epitaxial films *Appl. Surf. Sci.* **388** 557–64
[25] Van de Walle C G 1998 DX-center formation in wurtzite and zinc-blende $Al_xGa_{1-x}N$ *Physical Review B* **57** R2033
[26] Zhang G *et al* 1997 Relationship of background carrier concentration and defects in GaN grown by metalorganic vapor phase epitaxy *Appl. Phys. Lett.* **71** 3376–8